Journal of Sound and Vibration 329 (2010) 509–526

Contents lists available at ScienceDirect

Journal of Sound and Vibration

journal homepage: www.elsevier.com/locate/jsvi

Friction-induced vibration: Quantifying sensitivity and uncertainty

T. Butlin *, J. Woodhouse

Cambridge University Engineering Department, Trumpington Street, Cambridge, CB2 1PZ England, UK

ARTICLE INFO

Article history:
Received 7 May 2009
Received in revised form
16 September 2009
Accepted 16 September 2009
Handling Editor: H. Ouyang
Available online 17 October 2009

ABSTRACT

The limited success of predictive models of friction-induced vibration can, in part, be attributed to the inherent sensitivity of friction-coupled systems to variations, often uncontrolled, in parameter values such as the friction coefficient. This paper explores the sensitivity and uncertainty of predictions from a modal point of view, using models of a realistic complexity. A method for efficiently estimating prediction error bounds is presented and validated using representative parametric uncertainties. Measurement uncertainties are quantified providing an input for the error-bound analysis. Taken together, this forms the foundation for a direct comparison of predictions with experimental results from sliding contact tests.

1. Introduction

Experimental investigations of friction-induced vibration are often frustrated by results varying between nominally identical tests. This experience is true across the wide range of contexts that friction-induced vibration occurs, including wheel-rail noise and brake squeal. Predictive models also tend to be somewhat unsatisfactory: lumped parameter models are difficult to relate to real systems, and detailed finite element models do not account for many instances of high amplitude vibration. The development of this literature has been summarised by North [1], Ibrahim and Rivin [2], Kinkaid et al. [3] and Ouyang et al. [4].

This paper will explore some of the reasons for the difficulties commonly encountered. It is suggested that part of the problem lies with a high intrinsic sensitivity to uncertainties and that quantifying this sensitivity should be part of the specification of a useful predictive model. The study of sensitivity in friction coupled systems has begun to attract some attention (e.g. Guan et al. [5] and Huang et al. [6]), but this is usually within the context of design optimisation rather than model validation. The focus here is on integrating the combined effect of sensitivity and uncertainty on predictions.

In previous work (see Butlin and Woodhouse [7], Butlin [8]) the sensitivity and convergence behaviour was explored for simplified models. The results showed that predictions could sometimes be highly sensitive to parameters that are uncertain, are neglected as insignificant, or may vary with time. This paper presents a systematic methodology for quantifying the sensitivity and uncertainty of predictions and applies it to models of a more realistic complexity. This forms the foundation for a direct comparison of predictions with experimental results from sliding contact tests: Butlin and Woodhouse [8] provide an overview of the comparison with sliding contact tests and more detail is given by Butlin [9].

2. Theoretical framework

The generic system studied here is sketched in Fig. 1. A 'disc' is driven at constant velocity, V_0, and a 'brake' is pushed against it at a single point of contact with a dynamically varying normal force, N, composed of a steady equilibrium

* Corresponding author. Tel.: +44 1223 748522.
E-mail addresses: tb267@cam.ac.uk (T. Butlin), jw12@cam.ac.uk (J. Woodhouse).

0022-460X/$ - see front matter © 2009 Elsevier Ltd. All rights reserved.
doi:10.1016/j.jsv.2009.09.026

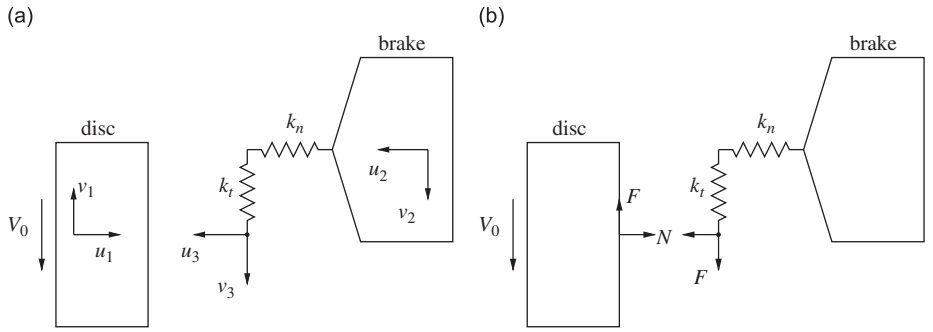

Fig. 1. Two linear subsystems coupled by a single point sliding contact with definition of variables. (a) Displacements. (b) Forces.

pre-load, N_0, plus a small fluctuating component such that $N = N_0 + N'e^{i\omega t}$. Similarly, the force tangential to the sliding direction due to friction, F, can be expressed as a steady equilibrium force, F_0, plus a fluctuating component such that $F = F_0 + F'e^{i\omega t}$. With a Coulomb friction law the normal and tangential forces are related by $F = \mu_0 N$ where μ_0 is the coefficient of friction. Consequently the sign of μ_0 defines the direction of rotation of the disc: if V_0 is positive then μ_0 is negative and vice versa. The normal and tangential displacements from equilibrium of the disc are denoted u_1 and v_1, respectively, and u_2 and v_2 for the brake. The normal and tangential displacements from equilibrium of the point of contact are denoted u_3 and v_3. The springs of stiffness k_n and k_t represent the linearised contact stiffness in the normal and tangential directions, respectively. Any damping that may result from the contact has been ignored.

The dynamics of the disc and brake can be described in terms of transfer functions:

$$\begin{bmatrix} u_1(\omega) \\ v_1(\omega) \end{bmatrix} = \begin{bmatrix} G_{11}(\omega) & G_{12}(\omega) \\ G_{21}(\omega) & G_{22}(\omega) \end{bmatrix} \begin{bmatrix} N'(\omega) \\ F'(\omega) \end{bmatrix}, \tag{1}$$

$$\begin{bmatrix} u_2(\omega) \\ v_2(\omega) \end{bmatrix} = \begin{bmatrix} H_{11}(\omega) & H_{12}(\omega) \\ H_{21}(\omega) & H_{22}(\omega) \end{bmatrix} \begin{bmatrix} N'(\omega) \\ F'(\omega) \end{bmatrix}, \tag{2}$$

where $G_{ij}(\omega)$ represent the disc's response and $H_{ij}(\omega)$ represent the equivalent responses for the brake. These transfer functions can be determined using standard vibration measurement techniques. The convention of the vibration literature is followed by using transfer functions defined as the Fourier transform of an impulse response, rather than the Laplace transform. To convert to the Laplace formalism the complex ω- plane should be rotated anticlockwise by 90° to correspond to the complex s-plane as $s = i\omega$.

Assuming a constant coefficient of friction leads to the characteristic function:

$$D = G_{11} + \mu_0 G_{12} + H_{11} + \mu_0 H_{12} + 1/k_n, \tag{3}$$

as derived by Duffour and Woodhouse [10,11]. The system is stable if and only if all the zeros of $D(\omega)$ have a positive imaginary part. The corresponding condition for stability in the Laplace formalism would require all the zeros to lie in the left half-plane.

If the frictional force is allowed to vary with the relative sliding velocity, a linearised friction law can be written:

$$F' \approx \mu_0 N' + i\omega\varepsilon N_0(v_1 + v_3). \tag{4}$$

The factor $i\omega$ converts the displacements v_1 and v_3 into changes in the relative sliding velocity. For further discussion of this friction model see Duffour and Woodhouse [11] and Butlin and Woodhouse [8]. Considering the transfer functions from any disturbance input (e.g. surface roughness or friction force perturbations) to any output (e.g. normal or tangential velocity) results in two characteristic functions:

$$E_1 = D + i\omega\varepsilon N_0[(G_{11} + H_{11} + 1/k_n)(G_{22} + H_{22} + 1/k_t) - (G_{12} + H_{12})^2] \tag{5}$$

and

$$E_2(\omega) = 1 + i\omega\varepsilon N_0(G_{22} + H_{22} + 1/k_t). \tag{6}$$

The system will be stable if and only if all the zeros of both $E_1(\omega)$ and $E_2(\omega)$ lie in the upper half-plane [11,7].

The characteristic functions (Eqs. (3), (5) and (6)) are in terms of transfer functions which can be measured. Fitting allows these functions to be approximately expressed as a modal summation (e.g. Skudrzyk [12]). For example, $D(\omega)$ can be written:

$$D = \sum_{\text{all } j \text{ (disc)}} \frac{g_{u_1}^{(j)} g_{u_1}^{(j)} + \mu_0 g_{u_1}^{(j)} g_{v_1}^{(j)}}{\omega_j^2 + 2i\zeta_j\omega_j\omega - \omega^2} + \sum_{\text{all } j \text{ (brake)}} \frac{h_{u_2}^{(j)} h_{u_2}^{(j)} + \mu_0 h_{u_2}^{(j)} h_{v_2}^{(j)}}{\omega_j^2 + 2i\zeta_j\omega_j\omega - \omega^2} + \frac{1}{k_n}, \tag{7}$$

where ω_j and ζ_j are the natural frequency and damping factor of the j th mode, respectively, of either the disc or the brake (if the uncoupled modes of both subsystems are sorted by ascending frequency, then the j th mode could correspond to either the disc or the brake). Mass normalised modal amplitudes that correspond to the disc subsystem are denoted g, and those for the brake h. As there is no mathematical distinction between the modal sums of the disc and the brake they can be combined. For convenience we define the modal coefficient $a_{pq}^{(j)}$ to represent the relevant product of modal amplitudes of either subsystem for the j th mode, such that we can rewrite $D(\omega)$ more simply:

$$D = \sum_{\text{all } j} \frac{a_{11}^{(j)} + \mu_0 a_{12}^{(j)}}{\omega_j^2 + 2\mathrm{i}\zeta_j\omega_j\omega - \omega^2} + \frac{1}{k_n}. \tag{8}$$

Finding the roots, once the model is truncated to a finite number of modes, requires solving the polynomial:

$$\sum_{\text{all } j}(a_{11}^{(j)} + \mu_0 a_{12}^{(j)}) \prod_{\text{all } k(\neq j)} (\omega_k^2 + 2\mathrm{i}\zeta_k\omega_k\omega - \omega^2) + \frac{1}{k_n}\prod_{\text{all } j}(\omega_j^2 + 2\mathrm{i}\zeta_j\omega_j\omega - \omega^2) = 0. \tag{9}$$

In the same way, the characteristic functions E_1 and E_2 can be expressed as polynomials.

In this paper, results will be presented to show the sensitivity of the roots of Eqs. (3), (5) and (6) to parametric variations. The approach to uncertainty estimation is illustrated by numerical studies using data gathered from a laboratory rig. This rig has also been used for a systematic series of sliding-contact tests [8,9]: those results do not form part of this paper but provide the background motivation. The sensitivity theory will be illustrated in terms of the particular transfer functions of this test rig, including measured estimates of the actual parametric uncertainty. The experimental work will be presented first, to set the scene for the sensitivity theory.

3. Experimental work

Figs. 2(a) and (b) show an overview of the pin-on-disc test rig used for the experimental work. A motor drives an aluminium disc in sliding contact with a polycarbonate pin, mounted on a support structure. The direction of rotation of the disc is defined by viewing the disc from the pin side: i.e. anticlockwise corresponds to the disc moving downwards relative to the pin (positive V_0). To provide a means of measuring the tangential vibration of the disc, and inputting

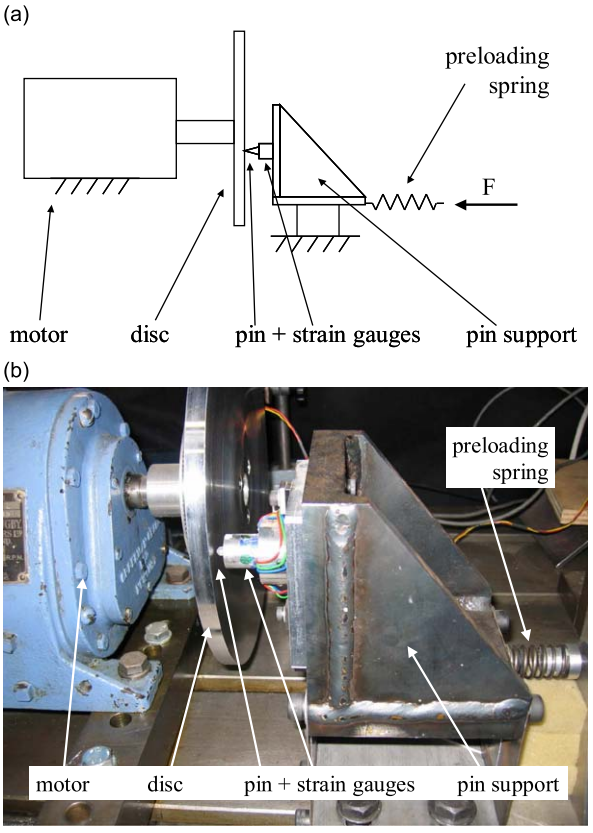

Fig. 2. The pin-on-disc test rig. (a) Schematic. (b) Picture.

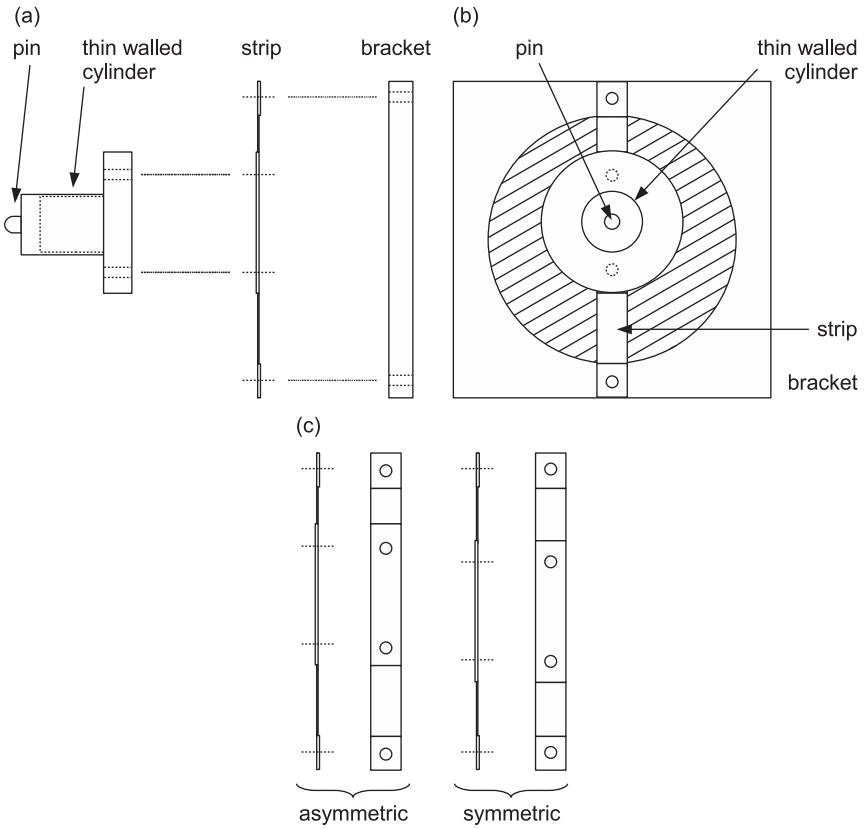

Fig. 3. The pin assembly. (a) Pin assembly: from side. (b) Pin assembly: from disc. (c) Asymmetric and symmetric metal strips.

tangential forces, a small metal stud was placed on the back face of the disc at the same radius as the point contact with the pin.

Fig. 3 shows a schematic of the pin assembly. The polycarbonate pin is screwed onto the dynamometer, a thin-walled cylinder mounted with strain gauges (see Smith [13]). This in turn is mounted on a thin strip of metal which is attached to a heavy support. The support is mounted on leaf springs. Two geometries of metal strips were manufactured: one asymmetrical and one nominally symmetrical. For a more detailed description see Duffour and Woodhouse [14].

3.1. *Measuring transfer functions*

There are two stages to the experimental work: measurement of the subsystem transfer functions to use for predictions, and sliding contact tests. This paper focusses on the transfer function measurements and their uncertainty, but the work described is in the context of a large number of sliding contact tests that were carried out in parallel over the course of one month (see Butlin [9] for a detailed discussion).

A nominal prediction requires a modal fit of the transfer function matrices of the pin and disc (Eqs. (1) and (2)). One aim of the test was to explore issues of repeatability and sensitivity, so the transfer functions of a variety of pin subsystems were measured and used for the sliding contact tests.

Two pin subsystems with fundamentally different dynamics were used: one was made nominally symmetric and the other deliberately asymmetric, about a plane through the point of contact perpendicular to the imposed sliding velocity. If both subsystems are symmetrical in this sense then $G_{12} = H_{12} = 0$, as the reflection about this plane reverses the sign of the off-diagonal terms while leaving the physical system entirely unchanged. Therefore within the scope of the linear, single-point contact framework used here (see Section 2 and Duffour and Woodhouse [10], Section 3), coupled symmetrical systems should not squeal unless the frictional forces are velocity dependent. The disc is symmetrical, and so significantly different behaviour is predicted from the symmetric and asymmetric pin subsystems.

To investigate sensitivity and explore the effect of uncertainties, perturbation masses were added to each system. In the case of the asymmetric pin assembly, the transfer function matrix was measured for no perturbation and a 1 g perturbation. In the case of the symmetric pin assembly, 4 and 14 g masses were also used. Fig. 4 shows pictures of the pin assembly with (a) no perturbation mass and (b) the 14 g mass. In each case the masses only came into contact with the

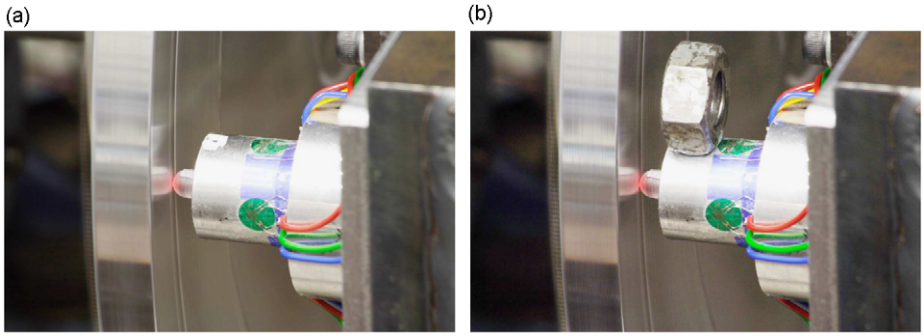

Fig. 4. Pictures of the pin assembly with (a) no perturbation mass and (b) a 14 g mass.

solid end of the dynamometer, not where the walls were thin. The masses were steel nuts placed on top of the solid part of the dynamometer using a minimal quantity of 'Blu-Tack' (a reusable putty-like adhesive). This crude attachment method enabled fast transition between cases and although the masses were not always placed in identical positions each time, this was simply regarded as part of the testing of the effect of uncertainties.

Each transfer function was measured at the beginning of the month of tests for each of the six cases: asymmetric pin with 0 and 1 g perturbations and the symmetric case with 0, 1, 4 and 14 g perturbations.

For a given transfer function, 40 repeat measurements were made and averaged. Each individual transfer function was stored in order to quantify the uncertainty inherent in any one measurement. Due to the imprecise positioning of a given perturbation mass, some uncertainty was inherent in its placement. Therefore the mass was repositioned between successive measurements so that this uncertainty was also quantified. This enabled direct comparison with sliding contact tests, where the masses were being changed between each test. A group of 40 measurements generally took approximately 10 min so variations with time would not be expected to be significant.

Ideally 40 repeat measurements under nominally identical conditions should yield identical transfer functions. It is of interest to consider why this is not the case in practice. One potential source is the variability of the precise nature of the hammer impulse between strikes. If the subsystem is indeed linear and time-invariant, the magnitude of the impulse should have no effect. Therefore non-linearity may be one factor as the impulse magnitudes were not tightly controlled. Another factor is likely to be the precise location of the contact between the hammer and pin. The hammer is fixed to a pendulum and carefully aligned but a small amount of 'play' in the pendulum mechanism means that there is room for slight differences in contact location between hits. Between groups of 40 measurements, a bigger effect is the difference in alignment of the hammer and laser: changes in contact location and angle of strike can both affect the modal amplitudes of the measured transfer functions. Over longer time-scales disassembly and reassembly of the pin subsystem when changing from an asymmetric to symmetric system or vice versa may also be significant. This was tested independently at the end of the four week test period.

The transfer functions should represent the linearised dynamics of the independent subsystems about the operating point during sliding. One difference between the uncoupled state and the actual operating state of the subsystems is that coupling will cause some pre-stress that may affect the relevant transfer functions. Such effects can be quantified by applying the pre-load through a soft coupling spring (see Butlin [9], Section 3.2.2). There is no difficulty in principle in including this in the theoretical framework used here, but for the present study the effects of pre-stress have not been included for simplicity.

With brake squeal occurring over a very broad frequency range the aim was to obtain transfer functions up to at least the audible limit of 20 kHz. Using a polycarbonate pin and a small metal-tipped impulse hammer (PCB 484B11), the pulse duration was too long to give a sufficient bandwidth. In order to obtain higher-frequency impact, the procedure used by Duffour and Woodhouse [14] was employed: the polycarbonate pin was replaced by a steel pin and the transfer functions were measured and fitted. It was confirmed that the main effect of changing the pin was to change the natural frequencies but not the modal amplitudes or damping factors. Hence the frequencies were found separately with the polycarbonate pin in place but striking just below on the steel dynamometer to obtain the same bandwidth. The duration of a hammer strike against steel was approximately 40 μs giving a bandwidth of 25 kHz. A sampling frequency of 100 kHz was used to log the data, avoiding any need for anti-aliasing filters which might distort the magnitude or phase. The gains of the amplifiers for the hammer and laser vibrometer were adjusted so that for a given test the signals were large enough not to be prone to significant quantisation noise.

3.2. Pin transfer function analysis

The detailed analysis of these measurements is somewhat complicated, so to orient the reader it is perhaps useful to preview the outcome of this section. The key results are given in Fig. 5, which shows the fitted poles for the pin subsystem

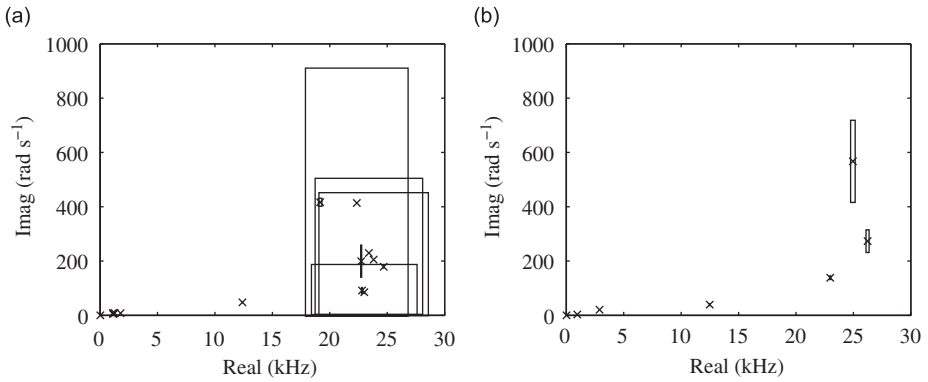

Fig. 5. Fitted complex poles of pin subsystem (×) with ±2 standard deviations uncertainty (rectangles). (a) Symmetric. (b) Asymmetric.

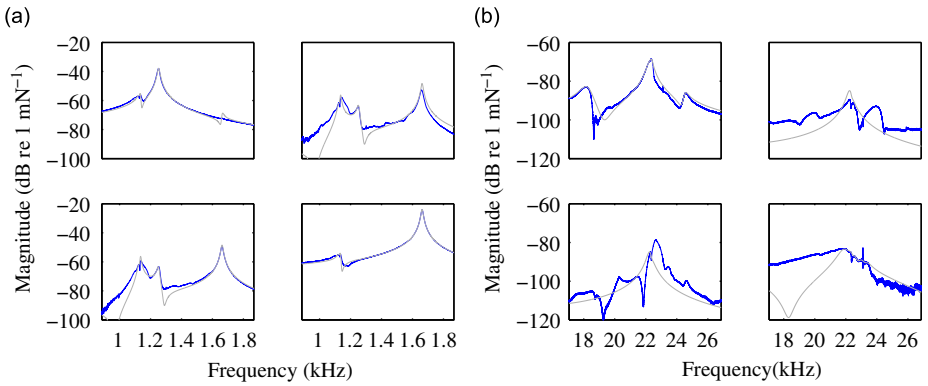

Fig. 6. Measured and fitted 2 × 2 matrix of transfer functions, **H**, for symmetric pin assembly. (a) Peaks near 1 kHz. (b) Peaks near 20 kHz.

together with their measured uncertainties for (a) the symmetric and (b) the asymmetric pin assemblies. The boxes represent plus or minus two standard deviations from the mean. These uncertainty bounds will form the input to the squeal sensitivity analysis to be presented in Section 4.

Fig. 6 (solid line) shows the matrix of transfer functions for the symmetric pin subsystem (with no perturbation mass) for two frequency ranges: (a) 1–2 kHz and (b) 17–27 kHz. Each transfer function shown is the average of 40 measurements. Although not visible in the chosen frequency ranges, any one transfer function spans approximately 100 dB (five orders of magnitude). Ideally there would be no cross-coupling between the two degrees of freedom if the pin subsystem were truly symmetrical. In reality the cross terms of the transfer function matrix are significantly smaller than the driving point terms (any given peak is approximately 20 dB lower), but they are not insignificant and cannot necessarily be discounted in predictions. This asymmetry is likely to result from a combination of imperfections in the pin assembly and misalignments of the hammer and vibrometer.

The first stage of the fitting procedure was to fit the peak regions of driving point terms of the averaged transfer functions using circle fitting, followed by iterative optimisation. The cross terms were identified using a simultaneous fit of the relevant three transfer functions beginning with the previous 'best' fit of the individual functions. This iteration was also done manually so that a good decision could be made as to which function could be considered most reliable.

At low frequencies the fit is reasonable: Fig. 6(a) shows the fitted (grey line) and measured (solid line) transfer functions for the four peaks near 1 kHz (only three peaks are obvious, but the first is a pair of very close peaks). Fig. 6(b) shows the same comparison for the peaks near 20 kHz. It can be seen that the fit is much poorer in this case. The cross terms are substantially different although the peak frequencies are still the same, and the 'best fit' only approximates the data close to the peaks for the driving point terms. Part of the discrepancy is due to higher frequency modes not being taken into account, especially the position and detailed shape of antiresonance troughs. In addition these modes are more non-proportionally damped, and hence have complex mode shapes, which are not taken into account in the fitting process used here. Also the high density of modes at these high frequencies begins to show the limitations of modal analysis. However, some care was taken to identify the most significant modes from the driving point terms and the increased uncertainty in this region has been taken into account as described below.

In order to estimate the uncertainty of any one transfer function the modal properties of all the identified modes of each of the 40 measured transfer functions were found using both circle fitting and rational fraction polynomial fitting. The

standard deviation as a percentage of the mean was then calculated for each parameter to quantify the uncertainty. The scatter for a given set of measurements is surprisingly large: Fig. 7 shows all 40 measurements of the first main peak of the driving point response, H_{11}, with the average superimposed in bold. The curves have been truncated at the −3 dB point of each (except for the average which has not been truncated).

The mean, standard deviation and standard deviation as a percentage of the mean are shown in Table 1 using both circle fitting and rational fraction polynomial (RFP) fitting. It can be seen that the natural frequency is very well defined with only a very small variation of 0.02 percent, while the damping factor varies by approximately 0.5 percent and the modal coefficient by 12 percent. It is interesting that the rational fraction polynomial fitting method more precisely identifies the damping factor of the mode, suggesting that this is a more reliable technique. This was also observed for most of the other modes, but not all, and so both methods have been used to estimate uncertainty: in general the lower percentage deviation has been used. Some modes were found to be highly uncertain, particularly small amplitude modes and those with high modal overlap. For some modes the frequency and damping factor varied significantly between the different terms of the transfer function matrix, so an estimate of the uncertainty was made based on the variation between the three functions.

The natural frequencies of the symmetric pin assembly are generally well defined, with the standard deviation usually well under 1 percent. The damping factor and modal coefficients are more variable with most standard deviations from 1–10 percent and 10–20 percent, respectively. These uncertainties have been calculated based on transfer function measurements with the metal pin and it is assumed that the uncertainty for each peak is unaffected by the change in mass.

The same procedure was carried out for the asymmetric pin assembly. The dynamics of this system turned out to be less ambiguous and the uncertainties were generally lower than for the symmetric assembly. The results have already been shown in Fig. 5. The difference is mainly for modes above 15 kHz, where many more small amplitude variations in the measured transfer functions were visible for the symmetric system (the measured transfer function in this frequency region is shown in Fig. 6(b)). This complicated the fitting process and resulted in many small amplitude modes being fitted: the difficulty in fitting these modes gives rise to the high uncertainty. Some of the differences between the asymmetric and symmetric systems could plausibly be attributed to differences in the boundary conditions (that depend on details of how the connecting bolts were assembled) resulting in different damping properties. Nevertheless it is not clear why the symmetric system should apparently have a higher modal density.

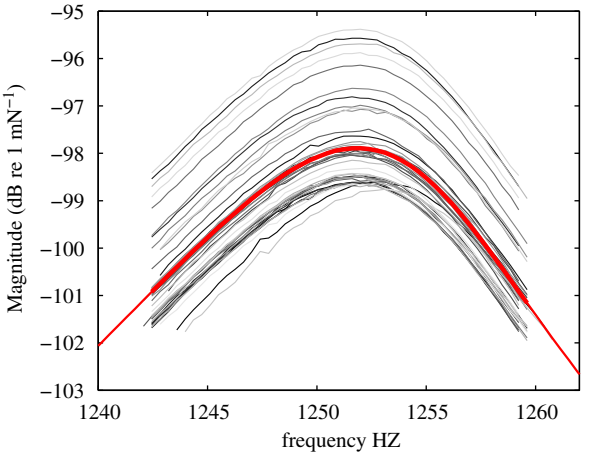

Fig. 7. Forty consecutive measurements of one peak of H_{11}. Each curve apart from the mean is truncated at the −3 dB point.

Table 1
Modal statistics of one peak of transfer function H_{11} for the symmetric pin assembly using circle fitting and rational polynomial fraction fitting.

	f_n (Hz)	ζ_n (ND)	a_n (kg^{-1})
Circle fitting			
Mean	1252.39	0.007	10.79
Standard deviation	0.25	0.00005	1.29
Percentage of mean	0.020	0.718	11.985
RFP fitting			
Mean	1251.58	0.007	10.68
Standard deviation	0.28	0.00002	1.25
Percentage of mean	0.022	0.319	11.706

The natural frequency is denoted by f_n, the damping factor by ζ_n and the modal coefficient by a_n.

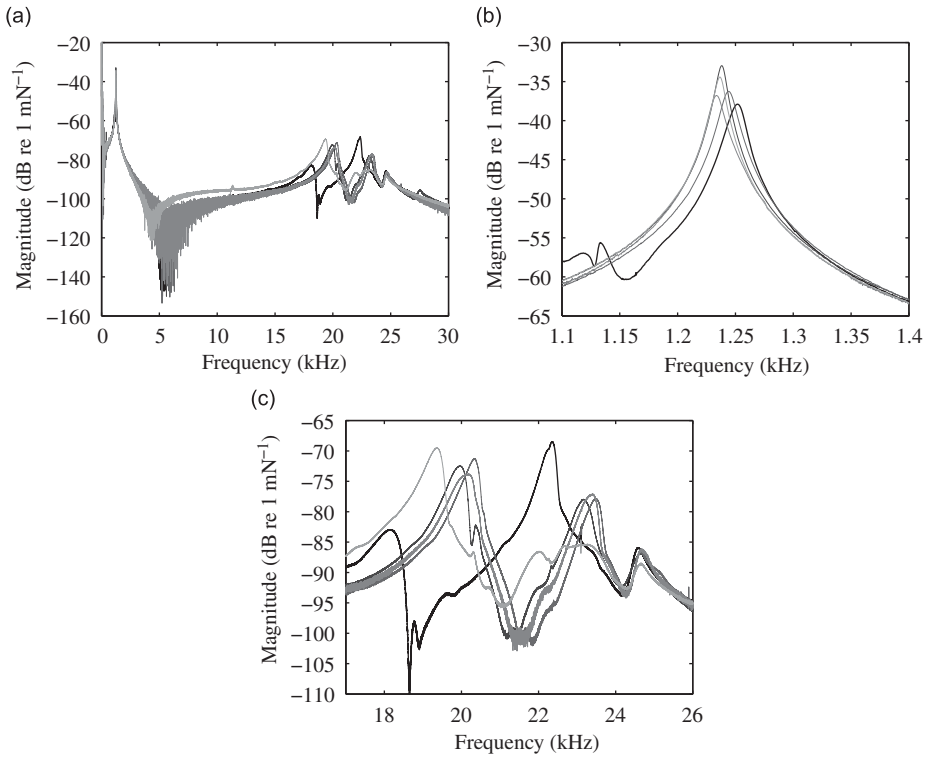

Fig. 8. Variation of transfer function H_{11} for symmetric pin assembly over four weeks. (a) 0–30 kHz. (b) Peaks near 1 kHz. (c) Peaks near 20 kHz.

The uncertainty considered so far only takes into account a given measurement on a particular day. Three further kinds of uncertainty have also been tested: (i) the variation with time has been checked by measuring the transfer functions at the start of each week and the end of all the tests, (ii) the scatter due to disassembly and reassembly has been quantified and (iii) the full matrix of transfer functions for each perturbation mass for both pin assemblies has been measured.

To quantify the variation in the transfer functions with time, the driving point response was measured for both pin assemblies each week over four weeks (in parallel with the sliding contact tests: Butlin and Woodhouse [8] and Butlin [9]). Fig. 8 shows each measured transfer function for the symmetric system, and Fig. 9 for the asymmetric system. In both cases the variation is fairly small at low frequencies (see Figs. 8(b) and 9(b)) but remarkably large at high frequencies (Figs. 8(c) and 9(c)). The differences between measurements at high frequencies are so large that in some cases it is not clear how the modes correspond, making attempts to take this into account rather difficult. The days on which each measurement was made is not shown on the plots as there is no obvious trend, suggesting that the disassembly and reassembly was the main factor governing variability.

Fig. 10 shows each of 20 consecutive measurements of the driving point response of the asymmetric pin assembly, where between each measurement all the bolts of the pin subsystem were loosened and tightened again. This seems to confirm that the dominant source of variation from week to week is due to the reassembly of the pin between sliding contact tests, rather than due to other time-dependent variations such as temperature cycles.

Fig. 11 shows the tangential driving point transfer function of the symmetric pin assembly for each of the perturbation masses in the frequency range 1.2–1.8 kHz. It can be seen that the perturbation masses have a systematic effect on the transfer functions and, as expected, frequencies decrease with increasing mass. The smallest perturbation mass of 1 g was usually found to change the transfer functions by a similar level as the uncertainty due to reassembly.

3.3. *Disc transfer function analysis*

The analysis carried out above for the pin subsystems was also carried out for the disc. The disc is much closer to being perfectly symmetrical than the symmetric pin assembly as the disc was machined in situ. While the stud (mounted on the disc to enable tangential measurements and inputs) breaks the symmetry and fixes the nodal lines, cross coupling between normal and tangential directions was small: the modal coefficients of the cross terms were generally between one and two orders of magnitude smaller than the dominant driving point term. The other effect of the stud (and other small departures from symmetry) is to separate the natural frequencies of each closely spaced doublet pair of modes.

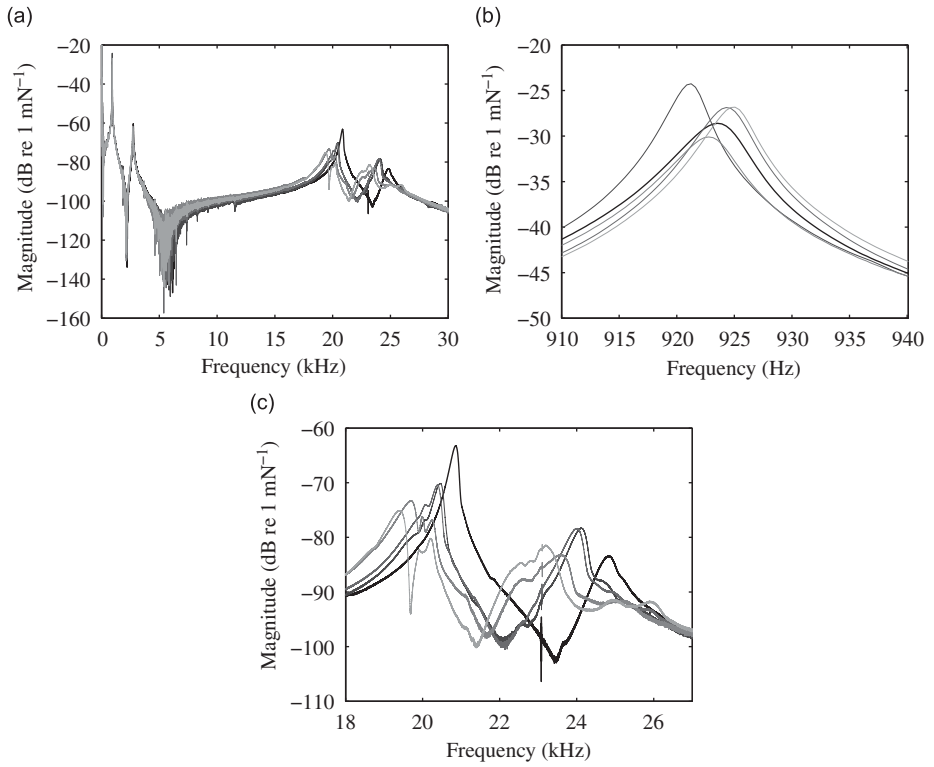

Fig. 9. Variation of transfer function H_{11} for asymmetric pin assembly over four weeks. (a) 0–30 kHz. (b) Peaks near 1 kHz. (c) Peaks near 20 kHz.

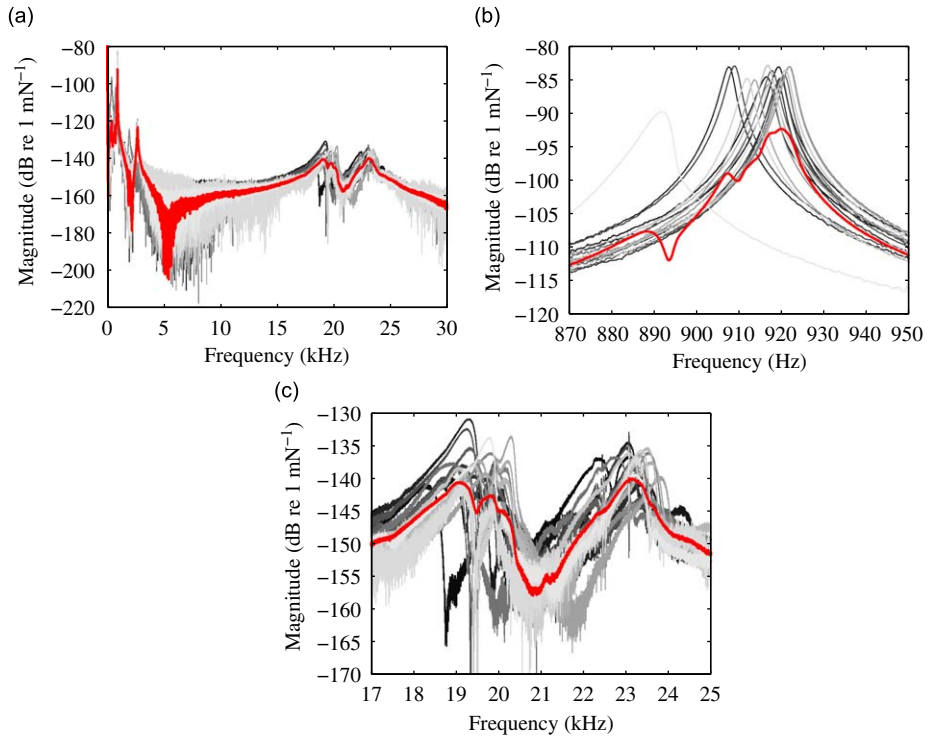

Fig. 10. Variation of transfer function H_{11} for asymmetric pin for 20 consecutive disassemblies and reassemblies. (a) 0–30 kHz. (b) Peaks near 1 kHz. (c) Peaks near 20 kHz.

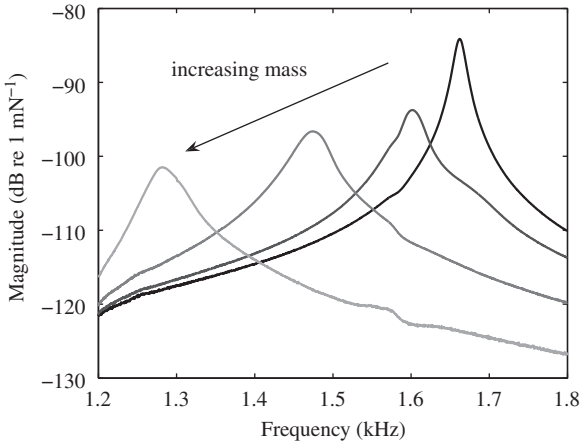

Fig. 11. Effect of perturbation masses on H_{22} for the symmetric pin assembly.

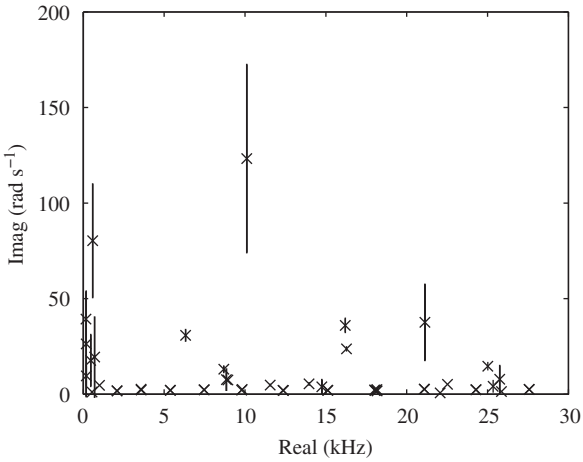

Fig. 12. Fitted complex poles of disc subsystem (×) with ±2 standard deviations uncertainty (rectangles).

For the present study the cross terms of the disc have been taken to be zero. The question can be raised as to whether this is a valid assumption in the light of Butlin and Woodhouse [7], which shows that small amplitude modes can sometimes be significant. However, further tests (described in Butlin [9]) suggest that the disc cross-terms do not significantly affect predictions in this case.

For the disc, a total of 44 modes were identified below 25 kHz (counting pairs as two modes). The corresponding complex poles are shown in Fig. 12 with the uncertainty for each pole shown by the rectangles (visible as lines because the frequency variation is so small). Typical frequency variations were of the order of 0.002 percent, while uncertainties in the other parameters were similar to those of the pin subsystem.

4. First-order perturbation analysis

The next step is to predict the effect of these parametric uncertainties on the zeros of the characteristic functions (equivalent to the poles of the coupled system). For highly simplified models this can be done analytically but as the complexity is increased it quickly becomes impossible. One method for estimating these error bounds is via a Monte Carlo approach: solve the characteristic function repeatedly using a range of parameter values representative of the uncertainty. For realistic systems there are a large number of defining parameters, making this approach computationally expensive. A first-order perturbation analysis, presented in this section, allows efficient assessment of the sensitivity of a nominal prediction with respect to each parameter separately. Such perturbation techniques have been used in a vibration context at least since Rayleigh [15]. For example, they have recently been applied in the context of friction-induced vibration by

Spelsberg-Korspeter et al. [16]. The technique is here applied to the theoretical framework of Section 2 in order to integrate it with the experimentally quantified uncertainties of Section 3.1, enabling prediction error-bounds to be estimated.

4.1. Eigenvalue perturbation analysis

The characteristic functions (Eqs. (3), (5) and (6)) can each be expressed as a polynomial as described in Section 2. It is possible to re-write a polynomial equation

$$s^N + p_{N-1}s^{N-1} + p_{N-2}s^{N-2} + \cdots + p_1 s + p_0 = 0 \tag{10}$$

as an eigenvalue problem: the polynomial roots are also the eigenvalues of its companion matrix $\mathbf{A}$ (e.g. Wilkinson [17]).

Given a perturbation $\mathbf{A} + \delta\mathbf{A}$ the change $\delta\lambda_i$ in an eigenvalue λ_i can be written:

$$\delta\lambda_i \approx \frac{\mathbf{y}_i^{\mathrm{T}}\delta\mathbf{A}\mathbf{x}_i}{\mathbf{y}_i^{\mathrm{T}}\mathbf{x}_i}, \tag{11}$$

where $\mathbf{x}_i$ and $\mathbf{y}_i$ are the corresponding eigenvectors of $\mathbf{A}$ and $\mathbf{A}^{\mathrm{T}}$, respectively.

The eigenvectors of $\mathbf{A}$ and $\mathbf{A}^{\mathrm{T}}$ can be shown to be

$$x_i = [\lambda_i^{N-1} \;\; \lambda_i^{N-2} \;\; \cdots \;\; \lambda_i \;\; 1]^{\mathrm{T}} \tag{12}$$

and

$$y_i = \begin{bmatrix} -\dfrac{\lambda_i}{p_0} \\ \dfrac{p_{N-2}}{p_0} + \dfrac{p_{N-3}}{\lambda_i p_0} + \cdots + \dfrac{p_1}{\lambda_i^{N-3} p_0} + \dfrac{1}{\lambda_i^{N-2}} \\ \dfrac{p_{N-3}}{p_0} + \dfrac{p_{N-4}}{\lambda_i p_0} + \cdots + \dfrac{p_1}{\lambda_i^{N-4} p_0} + \dfrac{1}{\lambda_i^{N-3}} \\ \vdots \\ \dfrac{p_3}{p_0} + \dfrac{p_2}{\lambda_i p_0} + \dfrac{p_1}{\lambda_i^2 p_0} + \dfrac{1}{\lambda_i^3} \\ \dfrac{p_2}{p_0} + \dfrac{p_1}{\lambda_i p_0} + \dfrac{1}{\lambda_i^2} \\ \dfrac{p_1}{p_0} + \dfrac{1}{\lambda_i} \\ 1 \end{bmatrix}. \tag{13}$$

The change in the companion matrix is

$$\delta\mathbf{A} = \begin{bmatrix} -\delta p_{N-1} & -\delta p_{N-2} & \cdots & -\delta p_1 & -\delta p_0 \\ 0 & 0 & \cdots & 0 & 0 \\ \vdots & \vdots & \ddots & \vdots & \vdots \\ 0 & 0 & \cdots & 0 & 0 \end{bmatrix}. \tag{14}$$

Using these results in Eq. (11) gives an expression for the rate of change of each polynomial root with respect to the polynomial coefficients and the nominal roots:

$$\frac{\partial\lambda_i}{\partial p_j} = \frac{\lambda_i^{j+1}}{\sum_{k=0}^{N-1}(N-k)p_k\lambda_i^k}. \tag{15}$$

4.2. Structure of perturbations

The above result requires knowledge of the structure of the polynomial perturbation, which is different for each of the uncertain parameters. The parameters considered for this analysis are the natural frequencies ω_n, the damping factors ζ_n, the modal coefficients $a_{11}^{(n)}$, $a_{12}^{(n)}$ and $a_{22}^{(n)}$, the coefficient of friction μ_0, the contact stiffnesses k_n and k_t, and the velocity-dependent friction term ε.

By way of illustration consider the simplest model with finite contact stiffness, using the characteristic function $D(\omega)$. The characteristic polynomial X can be written:

$$X = \sum_{m=1}^{M}(a_{11}^{(m)} + \mu_0 a_{12}^{(m)}) \prod_{p=1(\neq m)}^{M}(\omega_p^2 + 2\mathrm{i}\zeta_p\omega_p\omega - \omega^2) + \frac{1}{k_t}\prod_{p=1}^{M}(\omega_p^2 + 2\mathrm{i}\zeta_p\omega_p\omega - \omega^2) = 0. \tag{16}$$

If the modal coefficient a_{11}^k is perturbed such that $a_{11}^{(k)} \rightarrow a_{11}^{(k)} + \delta a_{11}^{(k)}$ then the perturbation to the polynomial will be

$$\delta X = \delta a_{11}^{(k)} \prod_{p=1(\neq k)}^{M} (\omega_p^2 + 2i\zeta_p \omega_p \omega - \omega^2). \tag{17}$$

The change in the root due to this perturbation can be found by combining Eq. (15) (the sensitivity to each polynomial coefficient) with Eq. (17) (the change in polynomial coefficients), noting that Eq. (17) needs to be normalised by the first polynomial coefficient to be consistent with Eq. (10). In this case the first coefficient is $1/k_n$ which remains unchanged and so this is straightforward to implement.

A perturbation of the contact stiffness such that $k_n \rightarrow k_n + \delta k_n$ results in a similar analysis, though slightly more care is required. The effect of the perturbation on $1/k_n$ is

$$\frac{1}{k_n + \delta k_n} \approx \frac{1}{k_n} - \frac{\delta k_n}{k_n^2}, \tag{18}$$

so the perturbation polynomial becomes

$$\delta X = -\delta k_n \frac{1}{k_n^2} \prod_{p=1}^{M} (\omega_p^2 + 2i\zeta_p \omega_p \omega - \omega^2). \tag{19}$$

In this case the first coefficient is also affected, which has an additional effect on the coefficients of the normalised polynomial δP:

$$\delta P = \frac{X + \delta X}{-c_1 - \delta c_1} - \frac{X}{c_1} = \frac{(X + \delta X)(c_1) - X(c_1 + \delta c_1)}{c_1(c_1 + \delta c_1)} \approx \frac{\delta X c_1 - X \delta c_1}{c_1^2}, \tag{20}$$

where c_1 is the first coefficient of the polynomial X.

Similar analysis can be carried out for the characteristic functions $E_1(\omega)$ and $E_2(\omega)$. In order to use this analysis for error bound estimates, the complex change in each root can be calculated for each uncertain parameter. The sum of the absolute real and imaginary parts provides an upper bound estimate for each of the root displacements if the uncertainties considered are sufficiently small.

4.3. Effect of finite precision uncertainty

It has been seen that the reliability of predictions is sometimes limited by sensitivity to finite-precision scale perturbations of the characteristic polynomial coefficients. Eq. (15) can be used to obtain an estimate of the numerical uncertainty of the predictions. The effect of a perturbation to each polynomial coefficient is considered in turn, so that the perturbation polynomial for a finite precision scale change in the coefficient of ω^k is simply $\delta c_k \omega^k$ where $2^{-53} c_k < \delta c_k < 2^{-52} c_k$ for double precision floating point representation. Summing the absolute root displacements for a perturbation of each coefficient gives an upper bound estimate of the numerical uncertainty of the predictions. In this case real and imaginary components are not separated so that the estimate is more conservative.

Again care must be taken when considering a perturbation of the first coefficient. From Eq. (20) the effect is to make an equivalent perturbation of each of the other coefficients such that

$$\delta P = -\frac{X \delta c_1}{c_1^2}, \tag{21}$$

as δX is zero except for the first coefficient.

5. Application to measured transfer functions

The above analysis requires just one numerical evaluation of the nominal characteristic polynomial roots, making it several orders of magnitude more efficient than repeatedly evaluating roots. It also provides a different perspective on the reliability of predictions and clearer insight into the individual effects of each parameter uncertainty. Before considering these other benefits, the validity of the method must be tested.

5.1. Approximating perturbed pole locations

For each parameter perturbation a numerical validation was carried out. Fig. 13(a) shows a typical comparison for one predicted root near 3 kHz using $D(\omega)$ (Eq. (3)) and including uncoupled modes up to 5 kHz. The coefficient of friction was varied from 0.5 to 0.6 in 20 steps with the predictions calculated numerically for each value and represented by dots. The nominal prediction is shown as a circle while the final prediction by a cross. Superimposed as a triangle is the estimated final root location based on the perturbation analysis: it can be seen that there is very good agreement. Fig. 13(b) shows a similar comparison for the root near 1 kHz where there is much poorer agreement, but it is clear that the first-order

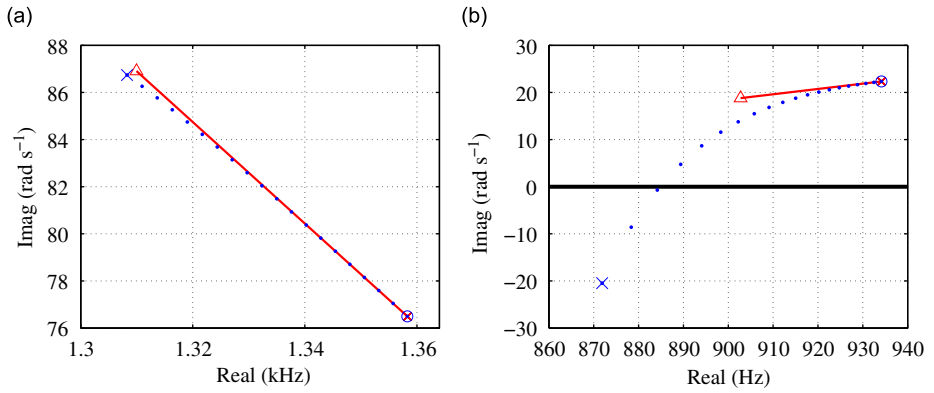

Fig. 13. Validation of first-order perturbation analysis: μ_0 varied by 20 percent. (◦) Nominal prediction for clockwise disc rotation with $\mu_0 = 0.5$; (×) perturbed prediction; (△) estimate of perturbed prediction. Model assumes infinite contact stiffness. (a) Root near 3 kHz. (b) Root near 1 kHz.

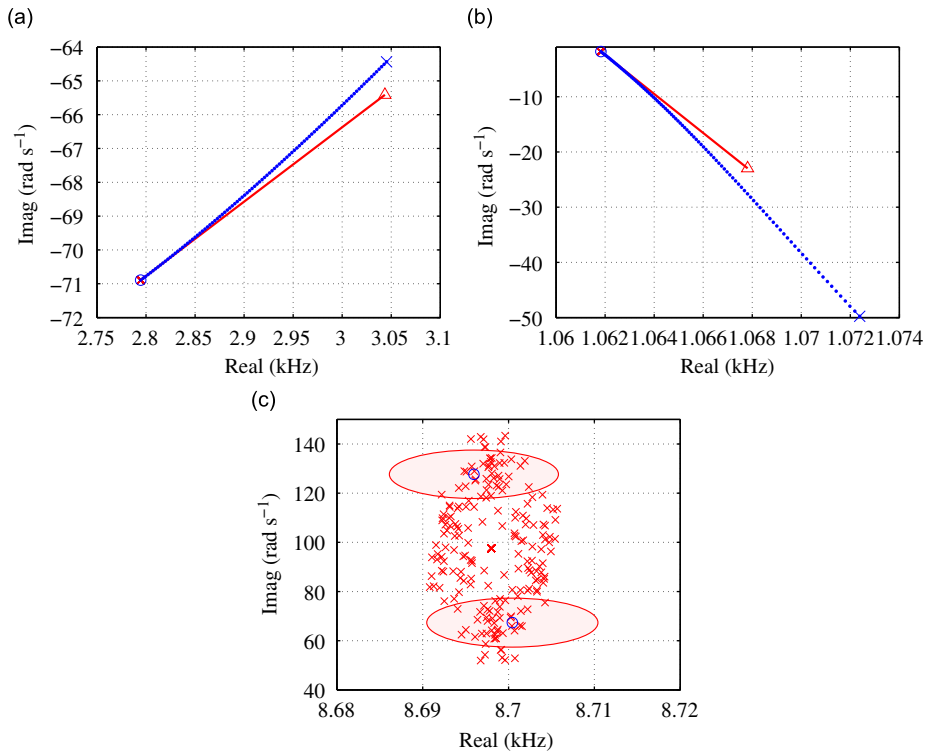

Fig. 14. Validation of first-order perturbation analysis: pin natural frequencies varied by 10 percent. (◦) Nominal prediction for clockwise disc rotation with $\mu_0 = 0.5$; (×) perturbed prediction; (△) estimate of perturbed prediction. Model includes finite contact stiffness ($k_n = 2 \times 10^6$ N m^{-1}) and velocity-dependent coefficient of friction ($\varepsilon N_0 = 10$ N s m^{-1}). (a) Root near 3 kHz. (b) Root near 1 kHz. (c) Numerical sensitivity. (ellipses) Numerical uncertainty estimate.

prediction is behaving as expected as the first-order prediction is tangential to the true root locus. The discrepancy arises because the perturbation is large and first-order terms become insufficient.

Another example is shown in Fig. 14 using the full model (including finite contact stiffness and a velocity-dependent coefficient of friction) with uncoupled modes up to 15 kHz. In this case all the pin natural frequencies have been perturbed together in uniform steps from 0 to 10 percent. Again two cases are shown: (a) shows a root for which there is good agreement while (b) shows a poorer first-order approximation. In both cases, however, the first-order solution is tangential to the path of the actual root.

The inclusion of higher frequency uncoupled modes for the case with a velocity-dependent coefficient of friction often results in numerical sensitivity. Fig. 14(c) shows the effect of finite precision scale perturbations of the polynomial coefficients (represented by a cluster of crosses) compared with the first-order estimate of their effect (represented by

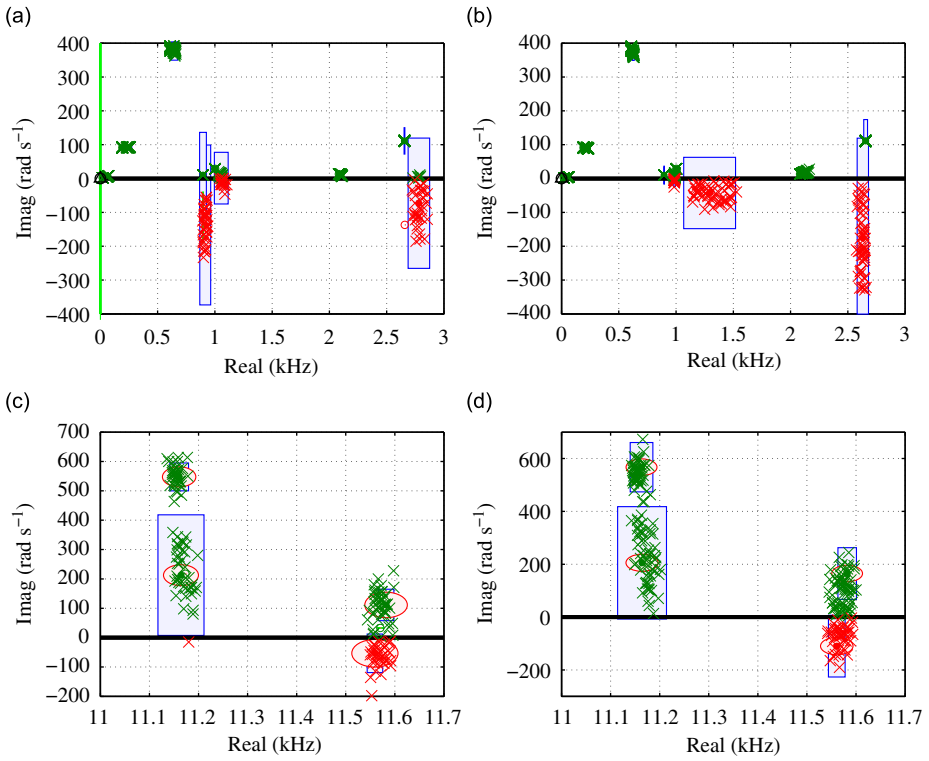

Fig. 15. Validation of first-order perturbation analysis: all parameters varied representatively ($f_n : 0.05$, $\zeta_n : 2$, $a_n : 10$ and $\mu_0 = 0.5 \pm 20$ percent). (•) Nominal prediction; (×) perturbed predictions; (shaded rectangles) error bound estimate; (shaded ellipses) numerical uncertainty estimate. Model includes finite contact stiffness ($k_n = 2 \times 10^6\,\mathrm{N\,m^{-1}} \pm 50$ percent) and velocity-dependent coefficient of friction ($\varepsilon N_0 = 10\,\mathrm{N\,s\,m^{-1}} \pm 50$ percent). (a) Clockwise, low frequency. (b) Anticlockwise, low frequency. (c) Clockwise, high frequency. (d) Anticlockwise, high frequency.

shaded ellipses). While the estimates do not encompass all the perturbed points, they are of the right order of magnitude and provide a very useful indication of when numerical sensitivity becomes significant. Again this is a more computationally efficient method than an explicit Monte Carlo approach.

5.1.1. *Estimating error bounds*

While the first-order method does not always give an accurate estimate of the root locations, particularly for large perturbations, the intention is to provide an efficient estimate of error bounds. When the effect of all uncertainties are included in the analysis then the worst case is unlikely: the differences between true and nominal values of each parameter are not expected to be the maximum estimated error bounds and their effect on predictions is unlikely to sum constructively. Therefore the first-order analysis is expected to give a practical and useful approximation of the possible root locations in the presence of these uncertainties.

Fig. 15 shows a comparison of the error-bounded predictions with repeated solutions of the characteristic equation E_1 using representative uncertainties. Each solution was calculated using nominal parameter values perturbed randomly with a uniform distribution over a representative range: $f_n = f_n \pm 0.05$ percent, $\zeta_n = \zeta_n \pm 2$ percent, $a_n = a_n \pm 10$ percent, $\mu_0 = 0.5 \pm 20$ percent, $k_n = k_t = 2 \times 10^6\,\mathrm{N\,m^{-1}} \pm 50$ percent and $\varepsilon N_0 = 10\,\mathrm{N\,s\,m^{-1}} \pm 50$ percent. Two groups have been focussed on to illustrate the results: low frequency clusters below 3 kHz and the groups near 11 kHz. Good agreement can be seen for both low and high frequency groups, with both numerical and parameter uncertainties being well accounted for. A similar verification has been carried out for the characteristic polynomial E_2 which also gives good agreement (not shown). The complete model was chosen for this verification as it represents the most sensitive case: predictions that did not include a velocity-dependent coefficient of friction were significantly more robust, revealing an inherent sensitivity to the choice of friction model.

5.1.2. *Breakdown of parameter contributions*

The first-order perturbation method for estimating prediction error bounds has been shown to be very effective, giving confidence that the effect of parameter uncertainties can be taken into account in a computationally efficient way. The method also provides a breakdown of the contribution of each parameter uncertainty to the uncertainty of any given root.

The relative sensitivity of each root with respect to fractional parameter changes can be found by making all perturbations an equal proportion of their nominal values. This provides some insight into the most significant parameters.

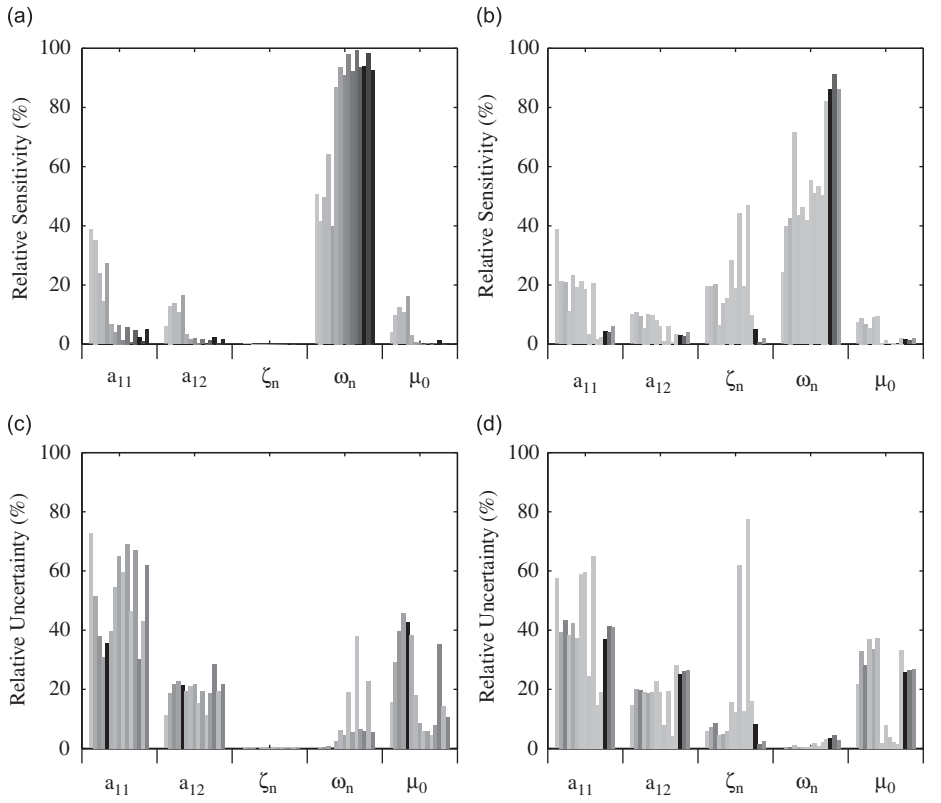

Fig. 16. Breakdown of parameter contributions to predicted roots: (a) sensitivity of real part, (b) sensitivity of imaginary part, (c) uncertainty of real part and (d) uncertainty of imaginary part. Each group of bars represents the contribution of the *x*-axis parameter to all the predicted roots. Each bar within a group is the contribution towards a particular root: within each group these are sorted in order of ascending frequency and are shaded according to the overall sensitivity of that root (dark shades correspond to high sensitivity).

An overall view of the contribution of each parameter to the relative sensitivities is shown in Figs. 16(a) and (b) using a model with infinite contact stiffness and neglecting a velocity-dependent coefficient of friction. The sensitivity of the real part of the roots is shown in (a) and the imaginary part in (b). Each group of bars represents the contribution of a parameter to the sensitivity of each of the predicted roots. The contributions of the modal parameters were calculated for each mode independently, then summed to give their overall contribution. Each bar within a group is the total contribution towards a particular root: within each group these are sorted in order of ascending frequency (left to right). The bars have been shaded according to the overall sensitivity of that root (dark shades correspond to high sensitivity).

Focussing on Fig. 16(a) it can be seen that the natural frequencies dominate the sensitivity of the real part of most predicted roots, contributing towards approximately 90 percent of the sensitivity for the higher frequency roots. The bars are darkest towards the right of each group, showing that in this case it is the high frequency roots that are most sensitive. The lower frequency roots are relatively more sensitive to the modal coefficients in addition to the natural frequencies, though overall these roots are more robust. The coefficient of friction has a relatively small effect, and the damping factor almost no effect on the real part of the roots.

Fig. 16(b) shows that the imaginary part of the predicted roots is more equally affected by each parameter: notably the damping factor has a much more significant role as might be expected. The root with the most sensitive imaginary part (the darkest bar in each group) is most sensitive to the natural frequency in this case, which contributes approximately 90 percent.

When finite contact stiffness is included in the model then fractional sensitivities are again dominated by the natural frequencies for the real part of the roots (not shown). The contribution to the imaginary part is again more equally split between all the parameters, though the natural frequencies and damping factors are more consistently influential. This remains true when a velocity-dependent coefficient of friction is included (with or without contact stiffness).

In addition it is interesting to look at the effect of representative parameter uncertainties on the prediction uncertainties. Figs. 16(c) and (d) show the relative contributions of each parameter uncertainty to the uncertainty of each predicted root for the real and imaginary parts, respectively. It can be seen that the real part is most affected by the 10 percent uncertainties in the modal coefficients but some of the high frequency roots are strongly affected by the 0.05 percent variation in the natural frequency (contributing up to approximately 35 percent of the overall uncertainty of one

root). It is interesting that the coefficient of friction, though significant, does not contribute more strongly to the overall uncertainty despite a 20 percent variation. The contribution breakdown is similar for the imaginary part of the roots, though the damping factor is much more important (contributing up to 80 percent of the overall uncertainty). The natural frequency now contributes very little to the overall sensitivity of the imaginary part, being a parameter that is more accurately defined.

The uncertainty breakdown when finite contact stiffness is included is shown in Fig. 17. In this case the uncertainty of the real part of many roots is affected most by the natural frequency uncertainties. However, the most sensitive roots overall (the bars shaded black) are most sensitive to the contact stiffness. The sensitivity of the imaginary part of the roots is affected most by the damping factors, though for the most sensitive root is more equally distributed between all the parameters. It is interesting that the modal coefficients play a weaker role with the inclusion of finite contact stiffness.

Fig. 18 shows the breakdown for a model with a velocity-dependent coefficient of friction but infinite contact stiffness. The uncertainty of the real part of approximately half the roots is dominated by the natural frequencies. The other roots depend most strongly on the modal coefficients and coefficient of friction. The imaginary part is affected by a wider distribution of parameters than before, though the most significant contribution is from the damping factors (varied by 2 percent) or the product εN_0 (varied by 20 percent).

Fig. 19 shows the case when both finite contact stiffness and a velocity-dependent coefficient of friction are included in the model. The root uncertainties are less affected by the modal coefficients, with strongest dependence on the natural frequencies for the real part. The imaginary part is generally affected most by damping factors, contact stiffnesses or the product εN_0. However, this case resulted in a high level of numerical sensitivity, so it is difficult to be clear to what degree these relative sensitivities can be trusted. The uncertainties for a model that just includes uncoupled modes below 5 kHz are shown in Fig. 20. This reveals a remarkably similar contribution from each parameter towards both real and imaginary parts of the roots.

This analysis reveals that no single parameter universally dominates prediction uncertainties, although trends indicate that natural frequencies are often significant for both real and imaginary parts, and damping factors contribute strongly to the imaginary part (which in turn determines stability). Including finite contact stiffness generally reduced the relative

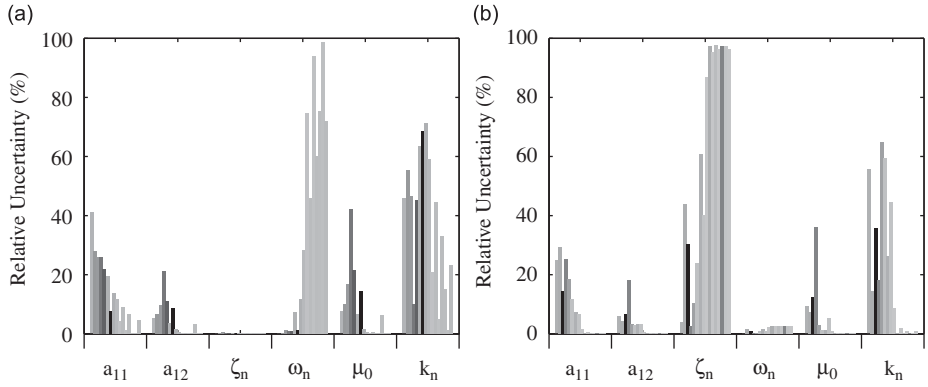

Fig. 17. Breakdown of parameter contributions to predicted roots. Model includes finite contact stiffness ($k_n = 2 \times 10^6\,\mathrm{N\,m^{-1}} \pm 50$ percent). (a) Uncertainty (real). (b) Uncertainty (imag).

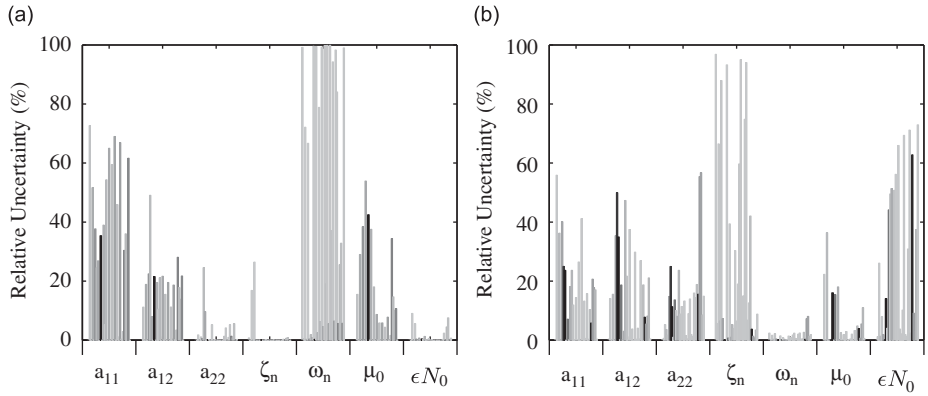

Fig. 18. Breakdown of parameter contributions to predicted roots. Model includes velocity-dependent coefficient of friction ($\varepsilon N_0 = 10\,\mathrm{N\,s\,m^{-1}} \pm 50$ percent). (a) Uncertainty (real). (b) Uncertainty (imag).

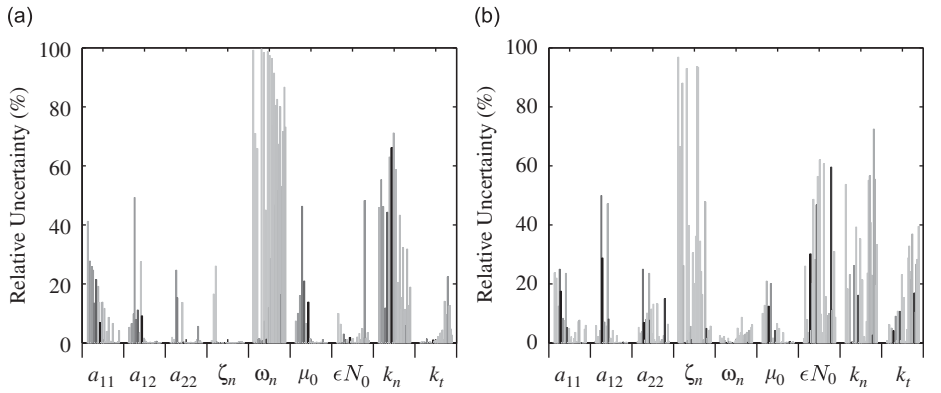

Fig. 19. Breakdown of parameter contributions to predicted roots. Model includes finite contact stiffness ($k_n = 2 \times 10^6\,\mathrm{N\,m^{-1}} \pm 50$ percent) and velocity-dependent coefficient of friction ($\varepsilon N_0 = 10\,\mathrm{N\,s\,m^{-1}} \pm 50$ percent). (a) Uncertainty (real). (b) Uncertainty (imag).

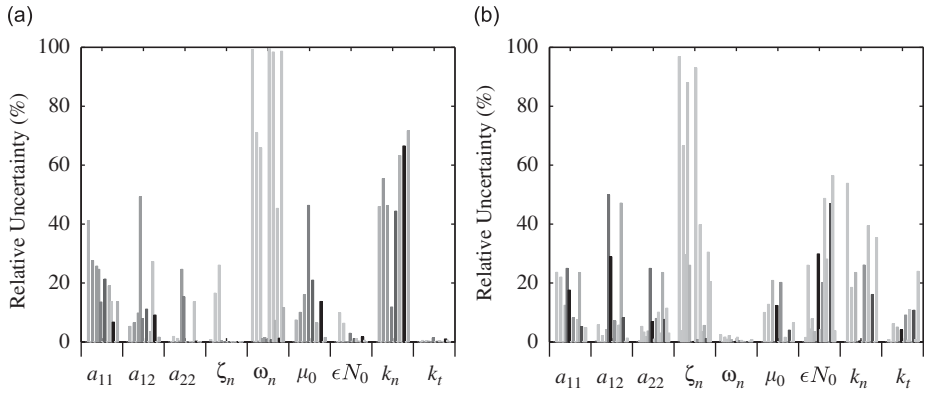

Fig. 20. Breakdown of parameter contributions to predicted roots. Model includes finite contact stiffness ($k_n = 2 \times 10^6\,\mathrm{N\,m^{-1}} \pm 50$ percent) and velocity-dependent coefficient of friction ($\varepsilon N_0 = 10\,\mathrm{N\,s\,m^{-1}} \pm 50$ percent), using only uncoupled modes below 5 kHz. (a) Uncertainty (real). (b) Uncertainty (imag).

contribution of modal coefficients towards uncertainties, suggesting that uncoupled pole locations are more significant than their amplitudes. However, care should be taken in making generalisations as the analysis has shown that each parameter sometimes contributes significantly towards uncertainties.

6. Conclusions

Attempts to validate models of friction-induced vibration are often limited by results varying under nominally identical conditions, suggesting that friction-coupled systems are intrinsically sensitive to parameter variations. This motivates a modelling approach that takes into account the effects of sensitivity and uncertainty on predictions. This article presents a framework for doing so from a modal viewpoint.

The uncertainty of transfer functions for a laboratory rig was quantified over different time-scales and for several similar systems, ready for making error-bounded predictions to compare with data from sliding contact tests. The uncertainties from consecutive measurements were perhaps surprisingly high even for high amplitude isolated modes. While natural frequencies were tightly clustered with a typical standard deviation of approximately 0.05 percent of the mean value, the damping factor typically had a 2 percent standard deviation and the modal amplitude of the order of 10 percent. The variations due to reassembly and over time were also quantified, and were found to be much bigger.

A first-order perturbation analysis was carried out to efficiently estimate the sensitivity of nominal predictions to parametric uncertainties. The method was shown to provide a useful estimate of error bounds when representative uncertainties were taken into account. It also provided a helpful estimate of numerical uncertainties in cases of ill-conditioning. The analysis allowed quantitative analysis of the relative contributions of each model parameter, which revealed that no single parameter could be identified as most important under all conditions. This perhaps contradicts the common folklore that uncertainty in friction is the main cause of the twitchiness of squeal.

This article focussed on integrating an uncertainty analysis into models of friction-induced vibration. Experimental estimates of parametric uncertainties, together with a first-order perturbation analysis, provided a basis for exploring the

effect of uncertainties on predictions. This forms the foundation for a more direct comparison with sliding contact test results than has previously been tried: results from these sliding contact tests are described in more detail by Butlin and Woodhouse [8] and Butlin [9].

Acknowledgement

Financial support from the EPSRC is gratefully acknowledged.

References

[1] M.R. North, Disc brake squeal, *IMechE Conference on Braking of Road Vehicles*, 1976.
[2] R.A. Ibrahim, E. Rivin, Friction-induced vibration, chatter, squeal, and chaos part II: dynamics and modeling, *American Society of Mechanical Engineers Applied Mechanics Reviews* 47 (1994) 227–253.
[3] N.M. Kinkaid, O.M. O'Reilly, P. Papadopoulos, Automotive disc brake squeal, *Journal of Sound and Vibration* 267 (2003) 105–166.
[4] H. Ouyang, N. Nack, Y. Yuan, F. Chen, Numerical analysis of automotive disc brake squeal: a review, *International Journal of Vehicle Noise and Vibration* 1 (2005) 207–231.
[5] D. Guan, X. Su, F. Zhang, Sensitivity analysis of brake squeal tendency to substructures' modal parameters, *Journal of Sound and Vibration* 291 (2006) 72–80.
[6] J. Huang, C.M. Krousgrill, A.K. Bajaj, Modeling of automotive drum brakes for squeal and parameter sensitivity analysis, *Journal of Sound and Vibration* 289 (2006) 245–263.
[7] T. Butlin, J. Woodhouse, Sensitivity of friction-induced vibration in idealised systems, *Journal of Sound and Vibration* 319 (2009) 182–198.
[8] T. Butlin, J. Woodhouse, Sensitivity studies of friction-excited vibration, *International Journal of Vehicle Design* 51 (2009) 238–257.
[9] T. Butlin, Prediction and Sensitivity of Friction-Induced Vibration, PhD Thesis, Cambridge University Engineering Department, 2007.
[10] P. Duffour, J. Woodhouse, Instability of systems with a frictional point contact—part 1: basic modelling, *Journal of Sound and Vibration* 271 (2004) 365–390.
[11] P. Duffour, J. Woodhouse, Instability of systems with a frictional point contact—part 2: model extensions, *Journal of Sound and Vibration* 271 (2004) 391–410.
[12] E.J. Skudrzyk, *Simple and Complex Vibratory Systems*, Pennsylvania State University Press, 1968.
[13] J.D. Smith, *Vibration Measurement and Analysis*, Butterworths, 1989.
[14] P. Duffour, J. Woodhouse, Instability of systems with a frictional point contact—part 3: experimental tests, *Journal of Sound and Vibration* 304 (2007) 186–200.
[15] J.W.S. Rayleigh, *The Theory of Sound (two volumes)*, second ed., Dover Publications, New York, 1894 1945 re-issue.
[16] G. Spelsberg-Korspeter, D. Hochlenert, O.N. Kirillov, P. Hagedorn, In- and out-of-plane vibrations of a rotating plate with frictional contact: investigations on squeal phenomena, *Journal of Applied Mechanics—Transactions of the ASME* 76 (4) (2009) 041006:1–15.
[17] J.H. Wilkinson, *The Algebraic Eigenvalue Problem*, Oxford University Press, Oxford, 1965.